




CALPHAD-based design and preparation of high-strength, high-conductivity Cu–Fe–Zr alloys

Huiya Yang^{1,2}, Tian Lv², Ye qiang Bu³, Jinming Wu¹, Youtong Fang³, Jiabin Liu^{1,3,*} , and Hongtao Wang^{3,*}

¹ State Key Laboratory of Silicon Materials, School of Materials Science and Engineering, Zhejiang University, Hangzhou 310027, People's Republic of China

² Shanghai Marine Diesel Engine Research Institute, Shanghai 200011, People's Republic of China

³ Center for X-Mechanics, Faculty of Engineering, Zhejiang University, Hangzhou 310027, People's Republic of China

Received: 12 August 2022

Accepted: 12 December 2022

Published online:

9 January 2023

© The Author(s), under exclusive licence to Springer Science+Business Media, LLC, part of Springer Nature 2023

ABSTRACT

A novel precipitation strengthening Cu–Fe–Zr alloy was designed and prepared based on the results of calculation of the phase diagram. After solid solutionizing, rolling and aging at 450 °C for 1 h, the alloy had a tensile strength of 515 MPa and an electrical conductivity of 72% IACS. There were two kinds of precipitates in the alloy after aging at 450 °C for 1 h. Fe precipitates with an average diameter of 4.3 nm were present in the deformed grains. Fe₂Zr precipitates with an average diameter of 29.1 nm were present in the recrystallized grains. Both the Fe and Fe₂Zr precipitates had coherent interfaces with the Cu matrix. The precipitation kinetics and effects on the properties of the alloy were discussed. It is found that the cold rolling enhanced the driving energy of precipitation. The precipitation of Fe and Fe₂Zr had a dominant effect on the increase in electrical and mechanical properties of the alloy.

Introduction

High-strength and high-conductivity Cu alloys are promising materials for electrodes, contact wires, lead frames, etc. [1–3]. However, strengthening while maintaining high electrical conductivity (EC) in Cu alloys is a challenge since strengthening mechanisms inevitably reduce the EC [4]. Precipitation strengthening is the most promising way to achieve an optimized combination properties [5, 6]. The precipitated

particles can strengthen the Cu as well as improve the EC [7, 8].

Be [9], Ti [10, 11], Fe [12], Cr [13], Zr [14], etc., are typical elements which have precipitation strengthening effect in the Cu alloys. Among them, Fe has drawn much attention due to its low cost [15–17]. The Cu–Fe (3–12 wt.%) alloys show high strength of 400–1100 MPa, but the corresponding EC is below 55% IACS [18]. The cold-drawn Cu–20 vol.% Fe alloy owned a strength even high as 1100 MPa but a low

Handling Editor: P. Nash.

Address correspondence to E-mail: liujiabin@zju.edu.cn; htw@zju.edu.cn

EC of 42% IACS [19]. α -Fe and γ -Fe particles would be produced to harden the Cu–Fe alloys during aging [20–22]. As a result, Cu–1 wt.% Fe alloy exhibited a higher tensile strength (TS) (194 MPa) than pure Cu (131 MPa) [23]. However, the use of Cu–Fe alloy is restricted by its poor EC. Fe solution atoms deteriorate the EC of Cu–Fe alloys dramatically, and the solubility of Fe in Cu is much higher than other elements [24, 25]. Therefore, micro-alloyed binary Cu–Fe alloys were rarely used because of the limited strengthening effect and obvious decrease in EC. On the contrary, Cu–Zr alloy has a high electrical and thermal conductivities, due to that Zr has very limited solubility in Cu [14, 26]. The precipitates in binary Cu–Zr alloys are Cu–Zr intermetallic compounds, e.g., Cu_3Zr [14], Cu_4Zr [27], Cu_5Zr [28] and Cu_9Zr_2 [14]. Micro-alloyed Cu–0.12 wt.% Zr alloy was prepared by melting, solution treatment, cold deformation and aging [14]. The alloy had a high EC (89.4% IACS) but relatively low yield strength (YS) (169 MPa) and TS (271 MPa). Since the solid solubility of Zr in Cu is only ~ 0.13 wt.% [29–31], the precipitation strengthening effect of the micro-alloyed Cu–Zr alloy is very limited.

Previous studies [32–34] found that the addition of P could form Fe_2P or Fe_3P phases in Cu–Fe alloys, which enhanced the precipitation of solid solution Fe and recovered the EC. Cu–0.7 wt.% Fe–0.15 wt.% P had an excellent high TS (467 MPa) and a high EC (78% IACS) [32]. Then, can the Fe–Zr compound be formed in the Cu–Fe–Zr ternary alloys to prepare high-strength and high-EC Cu alloys? There were few studies about the Cu–Fe–Zr alloys containing high contents of Fe and Zr. A Cu–11.5 wt.% Fe–0.2 wt.% Zr alloy was prepared by casting, rotary swaging, rolling and cold drawing [35]. The alloy had a combination properties of 752 MPa TS and 61.4% IACS EC. The microstructure and properties of the micro-alloyed Cu–Fe–Zr alloys have never been studied.

Calculation of phase diagrams (CALPHAD) is a powerful method for designing new alloys [36]. Pandat is one of the most commonly used CALPHAD software for designing new alloys. Thermodynamic parameters of the phases in the Co-rich region of the Co–Al–Ni–W quaternary alloys were calculated using the Pandat software [37]. The calculated results agreed well with the experimental results. CoNi-based wrought superalloy was designed by using Pandat software [36]. The designed alloy exhibited a

higher mechanical property than the traditional Co-based superalloys. For Cu–Fe–Zr ternary system, although the ternary phase diagram has been studied in the past, little attention was focused on the Cu-rich corner with low Fe and Zr contents [38].

In this study, the Cu-rich corner of the Cu–Fe–Zr system was calculated using the Pandat software and the CALPHAD method. It is found that the Fe_2Zr compound could form in the Cu alloy. Based on the phase diagram calculation results, a Cu–0.18 wt.% Fe–0.14 wt.% Zr ternary alloy was designed and fabricated. High strength and high EC were simultaneously obtained in the alloy. The microstructure was characterized and the strengthening and conductive mechanisms of the Cu–Fe–Zr alloy were discussed.

Phase diagram calculation and experimental

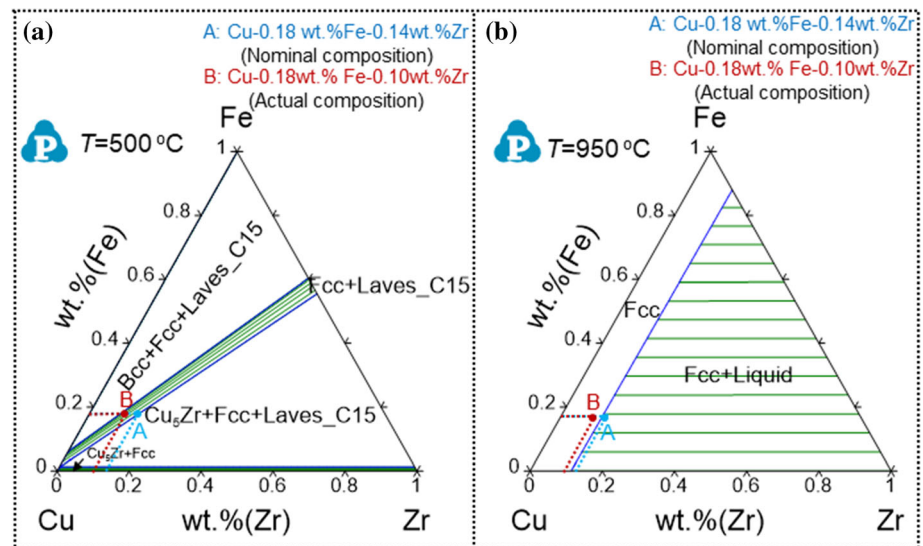
CALPHAD-based Cu–Fe–Zr alloy composition design

Phase composition calculations in the Cu–Fe–Zr alloy under equilibrium were performed using the Pandat software package. Figure 1a and b shows the isothermal cross section of the phase diagram at 500 °C and 950 °C, respectively [27, 29, 38, 39]. The green lines in the two-phase area of the phase diagram are the tie lines. The equilibrium phase of the alloy composition on each tie line is composed of the phases at both ends of the tie line. In the Cu–Fe–Zr alloy, we hope to obtain the Fe_2Zr precipitate only, so the alloy composition needs to be within the range of the two-phase (Fcc Cu + Lavas_C15 Fe_2Zr) region. Cu phase should be as pure as possible to ensure high EC in theory. Assuming the aging temperature is 500 °C (Fig. 1a), when the alloy composition falls on the bottom tie line of the two-phase region, the Cu phase is relatively pure. At the same time, the solubility of Zr in Cu is about 0.14 wt.% at 950 °C (Fig. 1b). Then, the ideal composition of the Cu–Fe–Zr alloy contains about 0.18 wt.% Fe and 0.14 wt.% Zr.

Experimental procedures

The Cu–Fe–Zr ingot was fabricated in an induction furnace under an Ar atmosphere using pure copper,

Figure 1 Isothermal cross section of the Cu–Fe–Zr phase diagram at a 500 °C and b 950 °C.



pure iron and pure zirconium. The actual composition of the ingot was measured to be Cu–0.18 wt.% Fe–0.10 wt.% Zr. The ingot was solution treated at 950 °C for different time and then cold rolled at room temperature to various reductions in thickness. Finally, the samples were annealed at 450, 500 and 550 °C for various time.

The microstructure, EC, hardness and TS of the samples were tested. The details of those testing methods could be found in previous studies [40, 41] for avoiding overlap.

Results

Figure 2 shows the metallographic (OM) structure of the samples in the as-cast state and solution treated at 950 °C. The spherical and granular primary phases are present in the Cu matrix in the as-cast alloy (Fig. 2a). The scanning electron microscopy (SEM) and energy-dispersive spectrometry (EDS) were conducted for the further characterization of the primary phases, as shown in Fig. 3. Points 1–3 in Fig. 3a mark the primary phases, and the EDS results show that the atom ratio of Fe/Zr is about 2 (Fig. 3b). So, the primary phase is deduced to be Fe_2Zr in the Cu–Fe–Zr alloy. Figure 2b–e shows that the diameters of the Fe_2Zr phase have a trend to decrease as the solution time increases. When solution treated at 950 °C for 12 h, the Fe and Zr elements are completely dissolved into the Cu matrix. The sample is in a supersaturated solid solution state (Fig. 2f).

Therefore, the optimized solution process is solid solution at 950 °C for 12 h.

After solution treatment at 950 °C for 12 h, the samples were subjected to cold rolling. The grains are elongated after cold rolling compared to the solid solution state (Fig. 4). The heavier the cold rolling deformation, the longer the grains. Besides, the deformation zone appears in the Cu matrix after cold rolling. The deformation zone is a local area where the crystals split from a single orientation into two complementary orientations due to the grain orientation and certain stress conditions during deformation. As the thickness reduction increases from 40% to 60%, the area and density of the deformation zone increase (Fig. 4a and b). As the cold rolling continues, the density of the deformation zone increases and the grains in the deformation zone are preferentially divided and broken to form sub-crystals (Fig. 4c and d).

Figure 5 shows the changes in the properties of the Cu–Fe–Zr alloy aged at 450, 500 and 550 °C for different time. The EC of the sample increases quickly at the initial stage and then slowly at the late stage when aging at 450 °C (Fig. 5a). It is indicated that the second phases precipitate during aging to purify the Cu matrix and recover the EC. The rolled samples show faster ascent rates of EC at the early aging than the un-rolled samples and achieve higher EC at the late stage of aging. It is mainly because the cold rolling can promote precipitation. The difference in rolling reductions has little effect on the EC of the samples in the late stage of aging. As shown in

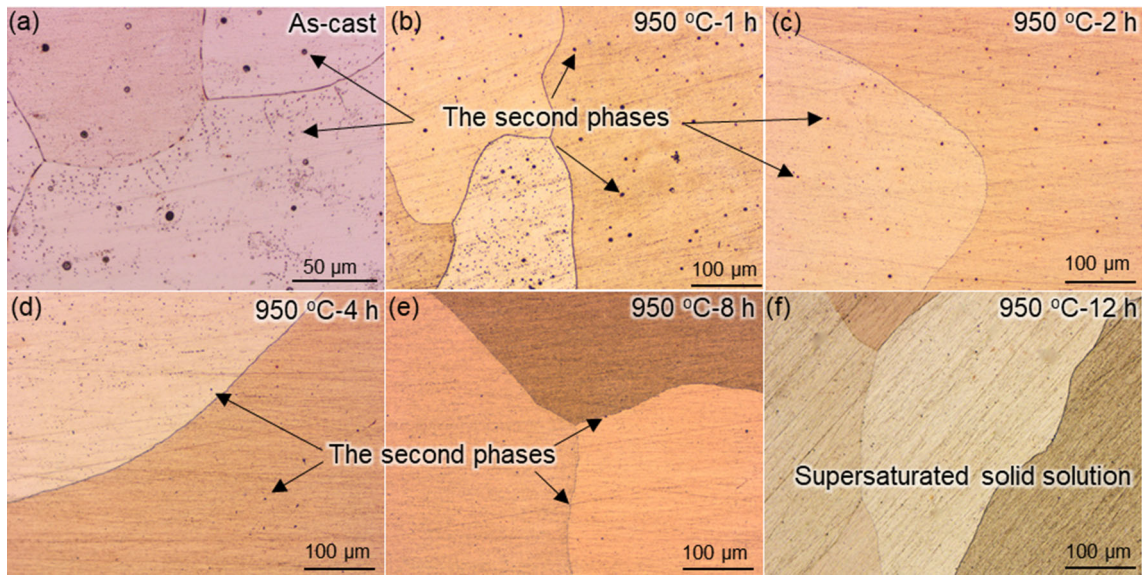
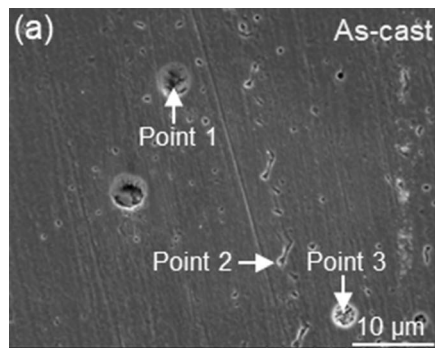


Figure 2 OM images of the samples **a** in as-cast state and solution treated at 950 °C for **b** 1 h, **c** 2 h, **d** 4 h, **e** 8 h and **f** 12 h.

Figure 3 a SEM microstructure of the sample in the as-cast state. **b** The second phase EDS composition results of the points marked in **a**.



Points	Cu (at.%)	Fe (at.%)	Zr (at.%)	Fe:Zr
1	88.18	8.31	3.51	2.37
2	92.03	5.23	2.74	1.91
3	85.13	10.55	4.32	2.44

Fig. 5b and c, the variations of the EC with the aging time of the samples aging at 500 and 550 °C show a similar tendency with that aging at 450 °C. Unlike the variations of the EC, rolling significantly improves the initial hardness of the sample (Fig. 5d–f). The larger the rolling reduction before aging, the stronger the work hardening effect and the higher the alloy hardness. From Fig. 5d, the hardness of the un-rolled sample and the samples rolled 40% and 60% increases rapidly at the early stage and then shows a slow increase rate. The samples rolled 80% and 90% have higher increase rates and higher hardness values at the initial aging stage, but show a hardness declining tendency at the over-aging stage. The declining tendency is mainly due to the softening effect related to the dislocation recovery, recrystallization and the precipitate coarsening at the over-aging stage [42]. As shown in Fig. 5e and f, when aging at 500 and 550 °C, the hardness of un-rolled and pre-rolled samples

both increases at the initial stage. However, the hardness of the un-rolled sample decreases at the over-aging stage, especially when aging at 550 °C. It is mainly because of the coarsening of precipitates at high-temperature aging. The hardness of the pre-rolled specimens aging at 500 and 550 °C decreases faster than that aging at 450 °C at the over-aging stage. The larger the rolling reduction, the faster the softening rate of the alloy.

The comprehensive EC-hardness properties of the specimens at different states are shown in Fig. 6a. The sample aged at 450 °C for 1 h after solid solution and cold rolled to a 90% reduction of thickness has the largest product value of hardness and EC. Therefore, the optimized preparation process of the Cu–Fe–Zr alloy is considered to be aging at 450 °C for 1 h after solid solution and 90% cold rolling. The corresponding comprehensive performance is 165 HV and 72% IACS. The sample shows the hardness

Figure 4 OM images of the samples cold rolled in the a 40%, b 60%, c 80% and d 90% reductions of thickness.

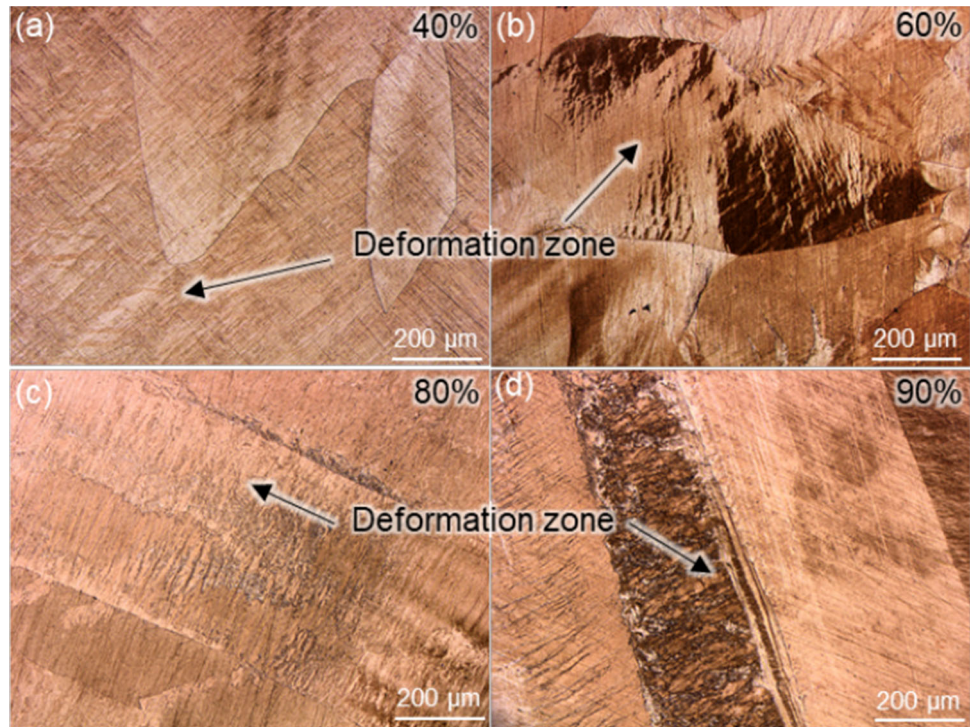
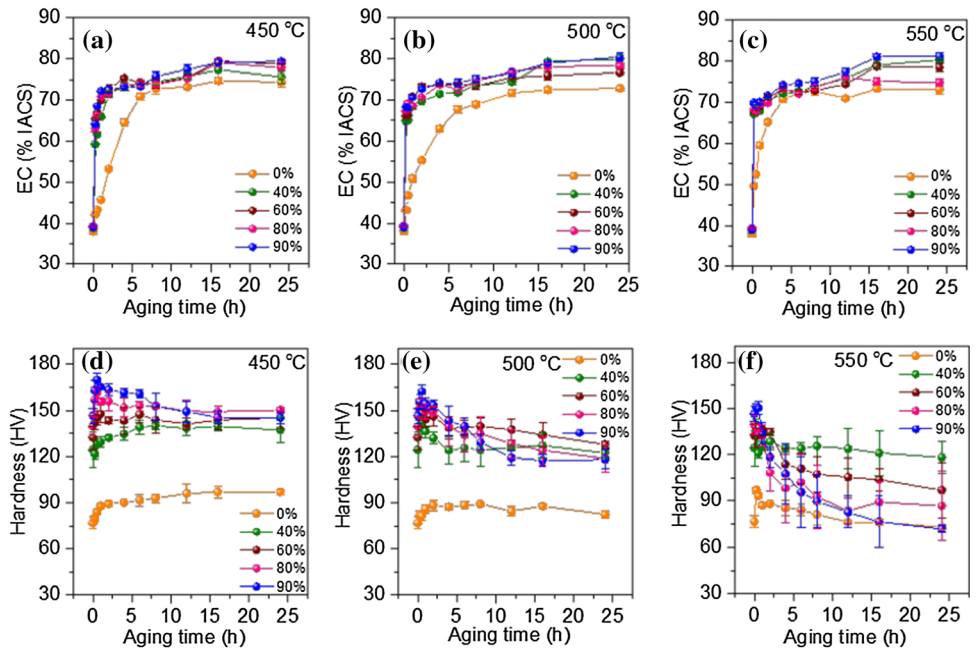


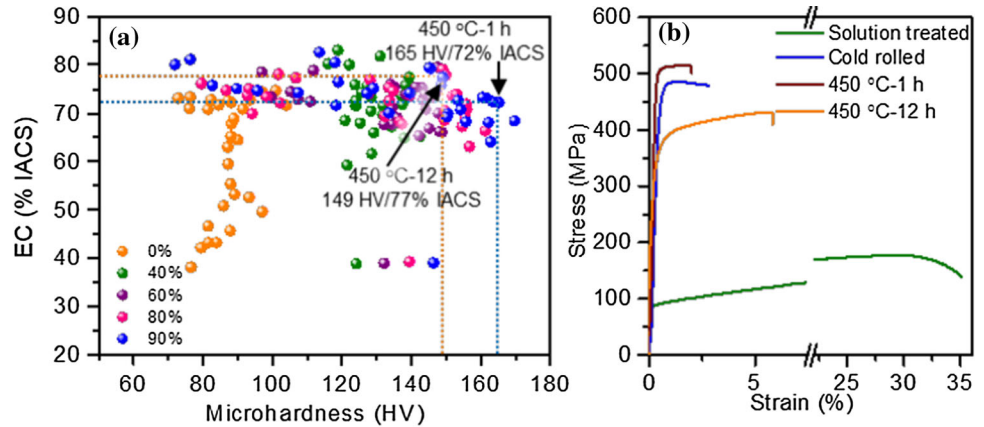
Figure 5 Variations of the EC and hardness with the aging time of the samples aged at 450, 500 and 550 °C. 0%, 40%, 60%, 80% and 90% represent the thickness reduction.



of 149 HV and EC of 77% IACS when aging at 450 °C for 12 h. Figure 6b shows the tensile properties of the samples subjected to different processes. The as-solution sample has the YS, ultimate TS and uniform elongation (UE) of 88 MPa, 179 MPa and 29%, respectively. After cold rolled to a 90% reduction of thickness, the YS and TS of the alloy reach 466 MPa

and 486 MPa, respectively. The UE of the alloy declines to 1% due to the deduction of plasticity caused by the work hardening. After aging at 450 °C for 1 h, the sample shows the YS, TS and UE of 508 MPa, 515 MPa and 2%, respectively. The increase in strength is mainly due to the second phase precipitate and brings about precipitation strengthening

Figure 6 **a** The combinative EC-hardness properties of the samples at different aged states. **b** Engineering stress–strain curves of the samples subjected to different processes.



effect after aging. The improvement in UE is mainly because of the dislocation recovery. After aging at 450 °C for 12 h, the alloy shows lower YS (348 MPa), lower TS (431 MPa) and higher UE (6%) than that aging for 1 h. It can be detected that the softening effect caused by dislocation recovery, recrystallization and precipitates coarsening is strong when aging for 12 h.

The electron backscatter diffraction (EBSD) characterization was conducted to investigate the grain structure of the rolled samples aged at 450 °C for 0 h, 1 h and 12 h. Figure 7a shows the inverse-pole-figure (IPF) map of the rolled sample. Different colors represent different grain orientations as indicated in the inset of Fig. 7a. The grain is elongated along the rolling direction (RD). The deformation zone parallel to the transverse direction (TD) distributes in the elongated grains. Figure 7b shows the distribution of grain determined from the IPF map. The grain size in the cold-rolled sample is uneven. There are both large crystal grains and small sub-crystals. Combined with Fig. 10b, it can be concluded that the sub-crystals are dislocation cells, which are caused by the increase in dislocation density during the plastic deformation. The average size of the sub-crystals (\bar{d}_{CR}) is 6.2 μm (Fig. 7d). The inset of Fig. 7c shows the misorientation angle map derived from the IPF map in Fig. 7a. According to statistics, the average misorientation angle (\bar{A}_{CR}) is 10.5°. The grain boundaries are mainly the low-angle grain boundaries (LAGBs, $< 10^\circ$), which are caused by the dislocation aggregation in the work hardening regions. High-angle grain boundaries (HAGBs) are mainly distributed in the deformation zone and sub-crystals regions.

Figure 8a shows the IPF map of the rolled sample aged at 450 °C for 1 h. Figure 8b shows the

distribution of grain determined from the IPF map. There are a large number of large-sized deformed grains still elongated along the RD which are not recrystallized. The deformation zone parallel to the TD still distributes in the elongated grains. The small-sized grains with an average diameter (\bar{d}_{A1}) of 6.6 μm (Fig. 8d) are formed by the dislocation recovery and recrystallization. The inset of Fig. 8c shows the misorientation angle map derived from Fig. 8a. The average misorientation angle (\bar{A}_{A1}) is 9.1°, and the grain boundaries in the alloy aged at 450 °C for 1 h are still mainly the LAGBs.

The EBSD results of the sample aged at 450 °C for 12 h are shown in Fig. 9. Figure 9a shows the IPF map, which indicates that the grains are still elongated along the RD but the inside deformation zone density is decreased. Compared Fig. 8b with Fig. 9b, the area of the deformed grains decreases, and the region of small-sized grains increases. Combined with Fig. 10f, the small-sized grains are recrystallized grains with an average diameter (\bar{d}_{A12}) of 6.1 μm (Fig. 9d). The misorientation angle map shows that the grain boundaries in the alloy aged at 450 °C for 12 h are still mainly the LAGBs and the average misorientation angle (\bar{A}_{A12}) is 9.0°. In summary, the cold-rolled sample and the samples aged at 450 °C for 1 h and 12 h are all composed of deformed grains and small-sized sub-grains. The grain boundaries are all LAGBs, and the alloy is not completely recrystallized during aging at 450 °C.

Transmission electron microscopy (TEM) characterizations were also conducted to investigate the deformed microstructure and recrystallized grains. Figure 10a indicates that the deformed grains are in a strip-shaped morphology with high-density

Figure 7 EBSD results of the cold-rolled sample. **a** EBSD IPF map (color orientation code shown in the bottom right corner). **b** Distribution of grain determined from the IPF map. **c** Misorientation angle map and distribution statistics result. **d** Grain diameter distribution in the black box in **b**.

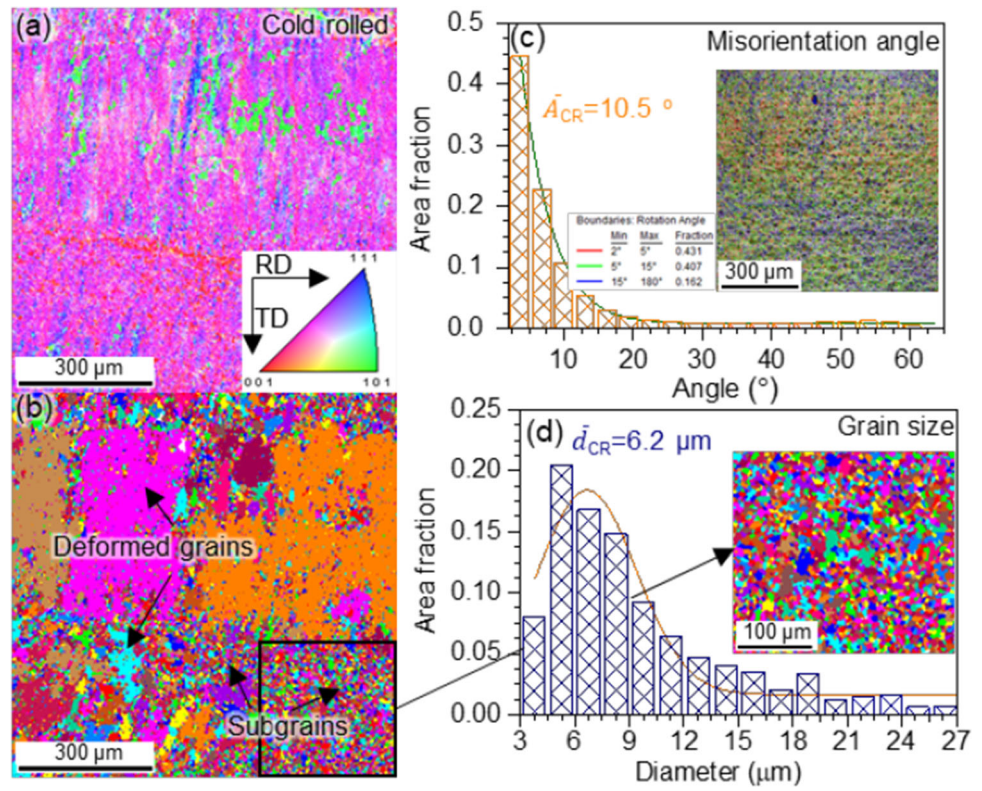


Figure 8 EBSD results of the sample aged at 450 $^\circ\text{C}$ for 1 h. **a** EBSD IPF map (color orientation code shown in the top right corner). **b** Distribution of grain determined from the IPF map. **c** Misorientation angle map and distribution statistics result. **d** Grain diameter distribution in the black box in **b**.

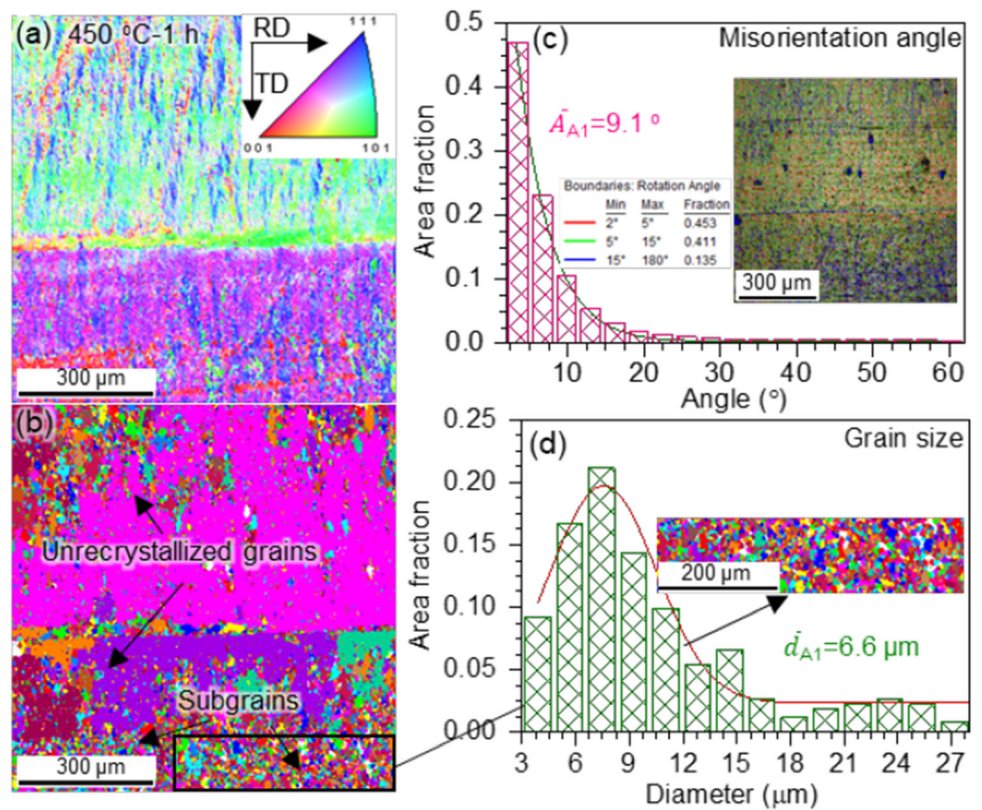


Figure 9 EBSD results of the sample aged at 450 °C for 12 h. **a** EBSD IPF map (color orientation code shown in the top right corner). **b** Distribution of grain determined from the IPF map. **c** Misorientation angle map and distribution statistics result. **d** Grain diameter distribution in the black box in (b).

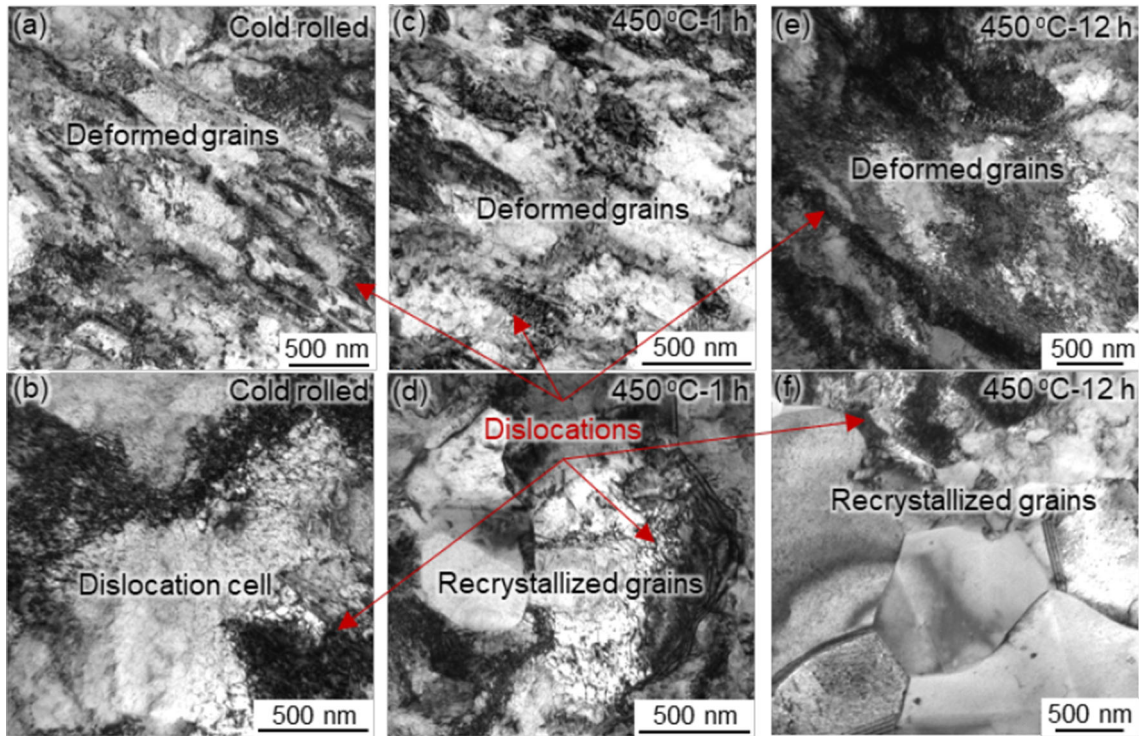
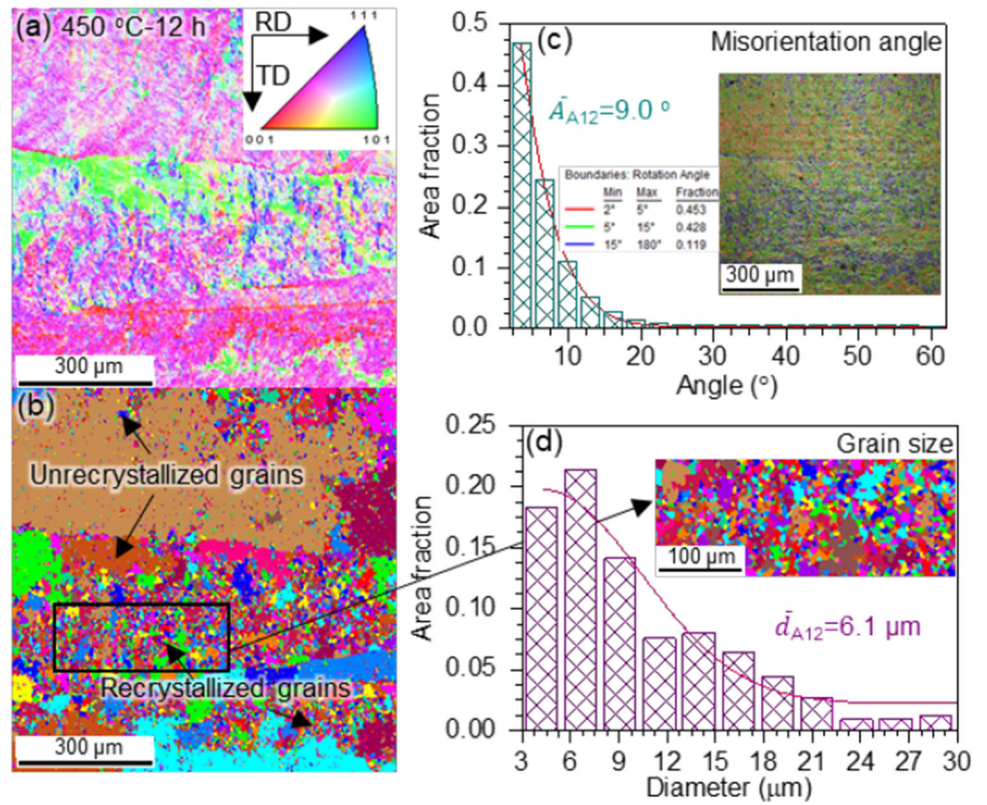


Figure 10 Bright-field TEM images of the (a, b) cold-rolled in a 90% reduction of thickness, (c, d) aged at 450 °C for 1-h and (e, f) aged at 450 °C for 12-h samples.

dislocations in the rolled samples. High density of dislocations entangle and form a cellular substructure shown in Fig. 10b. After aging at 450 °C for 1 h, the strip spacing of the strip-shaped deformed grains becomes wider (Fig. 10c), and few recrystallized grains appear in the Cu matrix (Fig. 10d). As the aging time increases, the deformed microstructure continues to recover. The strip spacing of the elongated grain becomes wider and more recrystallized grains arise in the samples aged at 450 °C for 12 h (Fig. 10e and f).

The sample aged at 450 °C for 1 h obtains the optimized properties of 165 HV hardness and 72% IACS EC. It is observed that deformed and recrystallized grains both exist in the sample. The deformed grain structure is further characterized by the scanning transmission electron microscopy (STEM). Figure 11a shows a scanning transmission electron microscopy-high angle annular dark-field (STEM-HAADF) image, showing high-density precipitates distribute in the Cu matrix. The corresponding EDS

mappings (Fig. 11a-1–a-4) indicate that the precipitates are rich in Fe, but poor in Cu and Zr. The average diameter of the Fe nanoparticles is as small as 4.3 nm (Fig. 11b). High-resolution STEM observation is conducted on the precipitates, shown in Fig. 11c. Figure 11c-1 is an inverse fast Fourier transform (IFFT) pattern of the area marked with the red box in Fig. 11c. It can be seen that the Cu/precipitate interface is fully coherent. The fast Fourier transform (FFT) pattern reveals that there is only one set of diffraction spots of Cu. This result also proves that Cu and nanoprecipitate have a coherent interface. The EDS mappings (Fig. 11c-3–c-5) indicate that the precipitates in the un-crystallized area are Fe particles.

There are different precipitates in the recrystallized grain in the specimen aged at 450 °C for 1 h. Figure 12a shows a STEM-HAADF image of the recrystallized grains and large-sized precipitates found in the Cu matrix. The precipitate density is decreased compared with that in the un-recrystallized area. The

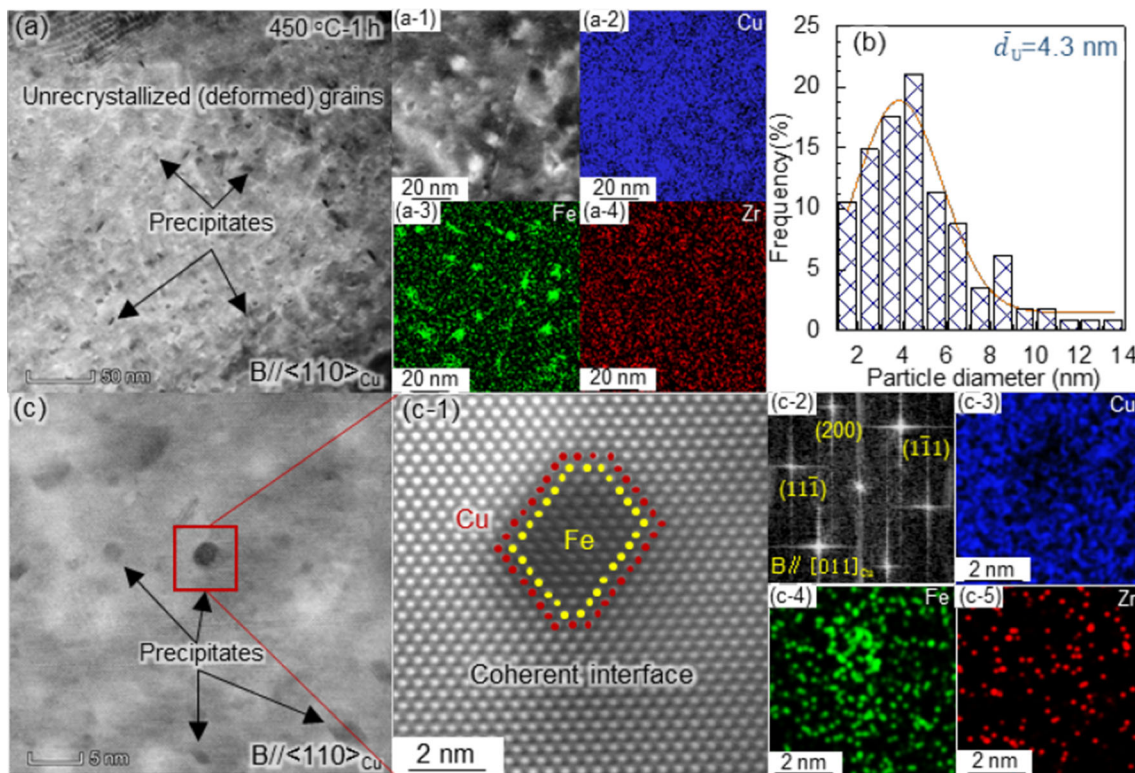


Figure 11 a, a-1 STEM-HAADF image of the deformed area in the sample aged at 450 °C for 1 h; Elemental mappings of a-2 Cu, a-3 Fe and a-4 Zr acquired from the area in a-1. b Precipitate diameters from the deformed area in the sample aged at 450 °C for 1 h. c STEM-HAADF image of the precipitates in the sample aged

at 450 °C for 1 h (taken from $\langle 110 \rangle_{Cu}$); c-1 IFFT pattern of the interface acquired from the area in c; c-2 FFT pattern and elemental mappings of c-3 Cu, c-4 Fe and c-5 Zr acquired from the area in c-1.

EDS mappings show that the precipitate is rich in Fe and Zr, but poor in Cu (Fig. 12b-1–b-4). Figure 12c-1 shows an FFT pattern of the area marked with the blue box in Fig. 12b-1. There is only one set of diffraction spots in the FFT pattern, indicating that the precipitate has the same crystal structure as the Cu matrix. Figure 12c-2–c-4 shows the IFFT pattern of the Cu/precipitate interface using only $(1\bar{1}\bar{1})_{Cu}$, $(11\bar{1})_{Cu}$ and $(200)_{Cu}$ reflections, respectively. No mismatch dislocation is found at the interface. It is revealed that the Cu/precipitate interface is coherent. The high-resolution STEM image of the precipitate is shown in Fig. 12d-1, and its corresponding FFT pattern is shown in the inset. The lattice parameter of the precipitate is measured to be the same as that of Cu. EDS result reveals that the atomic ratio of Fe to Zr is about 2. Figure 12d-2 shows an EDS line scan result, which also proves that the precipitate is Fe₂Zr in the recrystallized grains. According to statistics, the

Fe₂Zr particles have an average diameter of 29.1 nm, which is bigger than the particle diameter of Fe (4.3 nm) in the un-recrystallized grains.

Discussion

Precipitation kinetics

The phase transformation process of the alloy is reflected by the variation of EC, due to the sensitivity of EC to the precipitation behavior [43, 44]. Fe and Zr atoms are continuously precipitated as nanoparticles during the aging process. The volume fraction (*f*) of the Fe and Fe₂Zr precipitates at the aged time (*t*) can be expressed as [45]:

$$f = \frac{V_t}{V} \tag{1}$$

where *V_t* and *V* are the volumes of precipitates in a

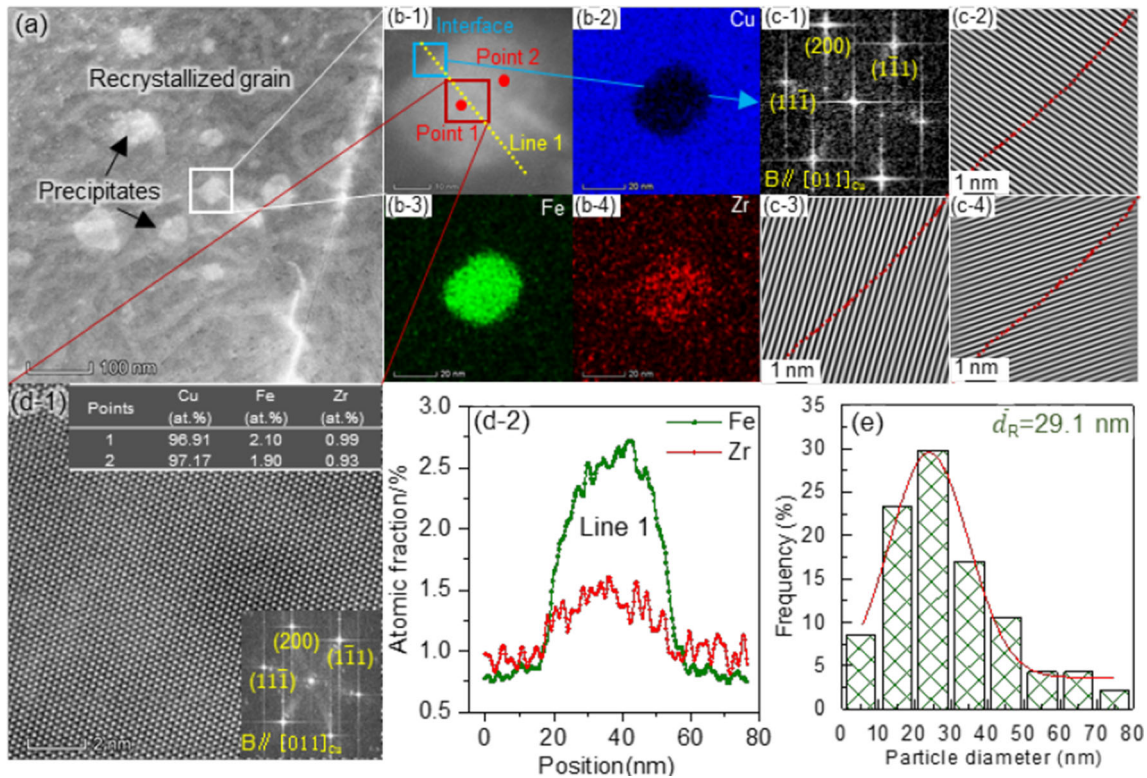


Figure 12 a, b-1 STEM-HAADF image of the recrystallized area in the sample aged at 450 °C for 1 h; elemental mappings of b-2 Cu, b-3 Fe and b-4 Zr acquired from the area in b-1. c-1 FFT pattern of the Cu/precipitate interface acquired from the area marked with the blue box in b-1. IFFT pattern of the Cu/precipitate interface using only c-2 $(1\bar{1}\bar{1})_{Cu}$, c-3 $(11\bar{1})_{Cu}$ and c-4 $(200)_{Cu}$ reflections. d-1 High-resolution STEM-HAADF

image of the precipitate acquired from the area marked with the red box in b-1; the corresponding FFT image is in the inset. d-2 EDS result of the Fe and Zr elements acquired from line 1 in b-1. e Distribution of the precipitate diameters determined from TEM images of the recrystallized area in the sample aged at 450 °C for 1 h.

unit volume of the Cu matrix after aging for t minutes and at the end of the aging process, respectively. $V_t = 0$ and $f = 0$ before phase transformation, and the EC of the rolled alloy can be defined as C_0 . The EC reaches the maximum C_{\max} when the precipitation process is finished. According to Matthiessen's rule [46], the EC of the alloy increases with f . The relationship between the C and the f can be expressed as a linear relationship, which is:

$$C = C_0 + \beta f \quad (2)$$

When phase transformation is finished, $C = C_{\max}$, $f = 1$, and then $\beta = C_{\max} - C_0$. The f at a certain time can be expressed as:

$$f = \frac{C - C_0}{C_{\max} - C_0} \quad (3)$$

Then, the f at any t can be calculated according to the EC of the alloy. The C and the f in the Cu–Fe–Zr alloy during aging at 450, 500 and 550 °C for different time are given in Table 1.

The kinetics Avrami equations of phase transformation can be expressed as [47]:

$$f = 1 - \exp(-bt^n) \quad (4)$$

where b and n are constants. Taking natural logarithms of both sides, then Eq. 4 can be expressed as:

$$\lg\left(\ln\frac{1}{1-f}\right) = \lg b + n \lg t \quad (5)$$

$\lg[\ln 1/(1-f)]$ and $\lg t$ have a linear function relationship, as shown in Fig. 13a. $\lg b$ is the intercept,

and n is the slope of the function line. Therefore, the phase transformation kinetics equation of the Cu–Fe–Zr alloy subjected to solid solution and then aging at 450, 500 and 550 °C can be expressed as:

$$f_{SA-450} = 1 - \exp(-2.20597t^{0.96736}) \quad (6)$$

$$f_{SA-500} = 1 - \exp(-1.74359t^{0.78945}) \quad (7)$$

$$f_{SA-550} = 1 - \exp(-1.12568t^{0.61570}) \quad (8)$$

The samples subjected to the solid solution, cold rolling (90% reduction of thickness) and then aging at 450, 500 and 550 °C can be expressed as:

$$f_{SRA-450} = 1 - \exp(-0.36058t^{0.29808}) \quad (9)$$

$$f_{SRA-500} = 1 - \exp(-0.20433t^{0.20807}) \quad (10)$$

$$f_{SRA-550} = 1 - \exp(-0.28896t^{0.25339}) \quad (11)$$

Relationships between the f and $\lg t$ are shown in Fig. 13b. The sample aging at 450 °C after solid solution shows an "S"-shaped kinetic curve which is typical of the diffusion phase transition. The precipitation rate is lower at the initial stage and higher at the later stage and then drops. The degree of Fe and Zr supersaturation in Cu acts as the precipitation driving energy [48]. The precipitation rates are higher when aging at 500 and 550 °C than at 450 °C. The higher aging temperature provides stronger precipitation driving energy for the nucleation and growth of Fe and Fe₂Zr phases. At the initial aging, the samples aging after solid solution and cold rolling show a much higher precipitation rate than the

Table 1 C and f of the alloy aging at different temperatures for different time

Samples	t (min)	0	15	30	60	120	240	360	480	720	960	1440
SA-450 °C	C	38.0	42.1	43.2	45.6	53.1	64.5	70.1	72.8	73.2	74.7	74.4
	f	0	0.11	0.14	0.21	0.41	0.72	0.90	0.95	0.96	1	0.99
SA-500 °C	C	38.0	43.1	46.7	50.8	55.3	63.0	67.7	68.9	71.7	72.4	72.8
	f	0	0.15	0.25	0.37	0.50	0.72	0.85	0.89	0.97	0.99	1
SA-550 °C	C	38.0	49.5	52.5	59.4	65.2	70.8	72.2	72.7	71.0	73.3	73.1
	f	0	0.33	0.41	0.61	0.77	0.93	0.97	0.98	0.93	1	0.99
SRA-450 °C	C	39.0	64.0	68.4	72.2	72.4	73.2	73.3	75.8	77.4	79.1	79.4
	f	0	0.62	0.73	0.82	0.83	0.85	0.85	0.91	0.95	0.99	1
SRA-500 °C	C	39.0	68.2	68.1	70.7	72.7	74.1	74.2	75.2	76.5	79.0	80.4
	f	0	0.71	0.70	0.77	0.81	0.85	0.86	0.87	0.90	0.96	1
SRA-550 °C	C	39.0	69.0	69.3	70.0	71.6	74.2	74.7	75.1	77.4	81.1	81.2
	f	0	0.73	0.72	0.73	0.77	0.83	0.84	0.85	0.91	0.99	1

SA the sample aging after solid solution treatment. SRA the sample aging after solid solution treatment and cold rolling

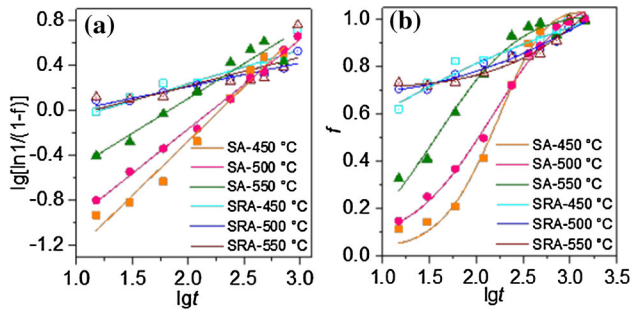


Figure 13 Relationships between **a** $\lg[\ln 1/(1-f)]$ and $\lg t$, **b** f and $\lg t$ of the samples aging at 450, 500 and 550 °C for different time. SA the sample aging after solid solution treatment. SRA the sample aging after solid solution treatment and cold rolling.

samples directly aging after solid solution. That is because the cold-rolling deformation introduces crystal defects, which provide more nucleation sites for precipitation [48, 49]. The rolling produces distortion energy in the crystal to increase the precipitation driving energy. At the later aging stage, the rolled samples have precipitation rates as low as that of the un-rolled samples. Besides the decrease in solute atom concentration, recovery and recrystallization also occur in the rolled samples after aging.

Precipitation behavior and its effects on the strength and EC

The precipitates in the deformed grains are Fe phases (Fig. 11) and in the recrystallized grains are Fe_2Zr phases (Fig. 12). The mean diameter of Fe is 4.3 nm and Fe_2Zr is 29.1 nm. The Fe and Fe_2Zr precipitates both have coherent interfaces with the Cu matrix. Previous studies [50–52] indicated that coherent metastable γ -Fe phases precipitated firstly in the microalloying Cu–Fe binary alloy. The γ -Fe would not transform into α -Fe until long-term aging or cold deformation [53]. The nucleation incubation period of the γ -Fe phase is very short, on the order of a few seconds [54]. However, the precipitation process of Cu–Fe alloy is very slow. Because the process is limited by the slow growth of γ -Fe, this is controlled by the slow diffusion of Fe atoms in Cu. To accelerate the precipitation of Cu–Fe alloy, two key parameters should be controlled: reducing the equilibrium solid solubility and increasing the diffusion coefficient of Fe in Cu [39, 55]. The first-principles calculation

results [55] showed that the Zr addition could increase the diffusion rate of Fe in Cu from $1.69 \times 10^{-14} \text{ cm}^2/\text{s}$ to $1.18 \times 10^{-12} \text{ cm}^2/\text{s}$. Our CALPHAD results indicate that Zr and Fe can form Fe_2Zr in Cu, which reduces the solid solubility of Fe in Cu at low temperatures. The experimental results confirm the precipitation of Fe_2Zr phases. As far as the Cu–Fe–Zr alloy precipitation sequence is concerned, the γ -Fe nucleates preferentially in the Cu matrix due to its short nucleation period. Then, the γ -Fe grows slowly and Zr gradually diffuses to it. The Zr accelerates the diffusion of Fe. Fe and Zr react and precipitate Fe_2Zr phases. The diffusion rate of Fe combined with Zr is accelerated, and the growth of the Fe_2Zr is accelerated. The coarsening of the precipitates is often accompanied by the recrystallization process [56]. Then, it can be seen that most of the precipitates at the recrystallization region are larger-sized Fe_2Zr . This precipitation process is similar to the precipitation of γ -Fe and coarse Fe_3P phases in the Cu–Fe–P alloy [33].

The precipitation of Fe and Fe_2Zr has a precipitation strengthening effect on the Cu–Fe–Zr alloy. The particle size and density of the precipitates and the relationship between dislocations and precipitates determine the precipitation strengthening effect [57]. The relationships between the dislocations and precipitates have two mechanisms: dislocation bypassing or cutting particles [58]. The former generally occurs when the precipitates are hard to shear or the phase interface is incoherent. The latter often takes place when the precipitates are soft and the precipitates have a coherent interface with the matrix [57]. Shi et al. [23] investigated the interactions between dislocations and Fe precipitates with a particle diameter of 5.5 nm in the Cu–1 wt.% Fe alloy. The coherent Fe particles hinder the dislocation movement by the cutting mechanism. The contribution of the cutting mechanism on the YS of Cu–Fe–Zr ($\Delta\sigma_p$) can be divided into two mechanisms: One is the coherency strengthening ($\Delta\sigma_c$), which operates by virtue of the elastic interaction between the strain fields of the coherent Fe particles and dislocations, and the other is the modulus hardening ($\Delta\sigma_m$), which occurs because of the shear moduli difference between the Cu and Fe phases. These mechanisms can be expressed as [59]:

$$\Delta\sigma_c = 2.6M(\varepsilon G)^{3/2} \left(\frac{2f_V r}{Gb} \right)^{1/2} \quad (12)$$

$$\Delta\sigma_m = 0.0055M(\Delta G)^{3/2} \left(\frac{2f_V}{Gb^2} \right)^{1/2} b \left(\frac{r}{b} \right)^{-1+3m/2} \quad (13)$$

where M is the Taylor factor; f_V is the volume fraction of Fe precipitates; G is the shear modulus of Cu; b is the Burgers vector; r is the radius of the habit plane; m is a constant; and ε and ΔG are the fractional misfit and difference of shear modulus between Cu and Fe precipitate, respectively. In contrast, the Fe_2Zr is recognized as an unsharable phase due to its super high hardness of 19.3 GPa [60]. Then, the increase in YS caused by the bypassing mechanism of Fe_2Zr ($\Delta\sigma'_P$) can be expressed by the Orowan–Ashby equation [61]:

$$\Delta\sigma'_P = \frac{0.81Mgb}{2\pi(1-\nu)^{1/2}} \cdot \frac{\ln(d_R/b)}{\frac{1}{2}d_R \left(\frac{3\pi}{2f'_V} \right)^{\frac{1}{2}} - d_R} \quad (14)$$

where ν is the Poisson's ratio and d_R and f'_V are the average diameter and volume fraction of the Fe_2Zr precipitates, respectively. Because Fe and Fe_2Zr precipitates exist simultaneously in the Cu matrix after aging at 450 °C for 1 h, it is hard to accurately calculate f_V , f'_V , $\Delta\sigma_P$ and $\Delta\sigma'_P$. But it is generally recognized that the coarsening of the precipitates will lead to the weakening of the strengthening effect [62, 63]. Then, in the alloy aging at 450 °C for 1 h, the Fe precipitates with smaller size and higher density have the dominant strengthening effect on the alloy. But the Zr addition enhances the precipitation of Fe, and the formation of Fe_2Zr also takes a key role in strengthening. The TS of the precipitation strengthening binary Cu–1 wt.% Fe alloy is only 194 MPa [23]. But in this work, the TS of the micro-alloyed Cu–0.18 wt.% Fe–0.10 wt.% Zr after aging at 450 °C for 1 h is as high as 515 MPa.

The effect of precipitation on the EC can be discussed with reference to the Matthiessen's law, and the electrical resistance of the Cu–Fe–Zr alloy (ρ) can be expressed as [64]:

$$\rho = \rho_{\text{Cu}} + \rho_{\text{D}} + \rho_{\text{P}} + \rho_{\text{S}} \quad (15)$$

where ρ_{Cu} is the electrical resistance of pure Cu. ρ_{D} , ρ_{P} and ρ_{S} are the electrical resistance caused by the defects (e.g., vacancy, grain boundary and dislocations), precipitates and solute atoms, respectively. Generally, defects have little effect on the EC, and ρ_{D}

is negligible to a certain extent [65]. The influence of the precipitates on the EC of the alloy (C) can be expressed as [66]:

$$C = C_M \left(1 + \frac{f}{\frac{1-f}{3} + \frac{C_M}{C_M - C_P}} \right) \quad (16)$$

where C_M is the EC of the matrix; C_P is the EC of the precipitates; and f is the volume fraction of the precipitates. In the precipitation strengthening high-strength and high-conductivity Cu alloys, C_P is usually much higher than C_M and f is less than 3 vol.%, and then, $C \approx 0.97 C_M$. It can be seen that the influence of precipitates on the EC is small. It is confirmed that the ρ_{S} is the primary factor that decreases the EC in precipitation strengthening Cu alloys [7], i.e., the EC of the alloy is mainly dependent on the purity of the Cu matrix [2]. Then, the more sufficient precipitation of the Fe and Zr solute atoms, the purer the Cu matrix and the higher the EC of the Cu–Fe–Zr alloy. After aging at 450 °C for 1 h, 82% of the Fe and Fe_2Zr particles precipitate (Table 1), resulting in the corresponding high EC (72% IACS) of the alloy. The electrical resistance of the alloy is mainly caused by the still solid solution of Fe and Zr atoms in the Cu lattice.

Conclusions

The Cu-rich corner of the Cu–Fe–Zr system was calculated using the Pandat software according to the CALPHAD method. It was predicted that Fe_2Zr can be precipitated in the Cu matrix. A novel system of Cu–0.18 wt.% Fe–0.14 wt.% Zr was designed and prepared with the reference to the CALPHAD results. The designed alloy had the excellent combination mechanical (hardness of 165 HV, YS of 508 MPa and TS of 515 MPa) and electrical properties (EC of 72% IACS). Two kinds of precipitates were found in the Cu alloy. The coherent Fe precipitates with a particle size of 4.3 nm were present in the deformed grains. The Fe_2Zr precipitates which also had coherent interfaces with the Cu had an average diameter of 29.1 nm, and they were formed in the recrystallized grains. The cold rolling enhanced the driving energy of precipitation. The precipitation of Fe and Fe_2Zr had a dominant effect on the increase in strength and EC of the alloy.

Acknowledgements

This work was supported by the National Natural Science Foundation of China (92266202) and the “Leading Goose” R&D Program of Zhejiang Province (No. 2023C01080).

Author contributions

HY was involved in investigation, writing—original draft, writing—reviewing and editing. TL was involved in reviewing and editing. YB was involved in investigation. JW and YF were involved in supervision. JL was involved in supervision, resources, writing—reviewing and editing. HW was involved in supervision and resources.

Declarations

Conflict of interest The authors declare that they have no known competing financial interests or personal relationships that could have appeared to influence the work reported in this paper.

Data availability The raw/processed data required to reproduce these findings cannot be shared at this time as the data also form part of an ongoing study.

References

- [1] Zhang K, Yang JJ, Li JY, Chen XH, Zhou HL, Liu P (2021) Effect of deformation and aging treatment on the microstructure and properties of Cu-0.45 Cr-0.14 Ti (wt.%) alloy. *J Alloys Compd* 851:156776. <https://doi.org/10.1016/j.jallcom.2020.156776>
- [2] Lei Q, Li Z, Gao Y, Peng X, Derby B (2017) Microstructure and mechanical properties of a high strength Cu–Ni–Si alloy treated by combined aging processes. *J Alloys Compd* 695:2413–2423. <https://doi.org/10.1016/j.jallcom.2016.11.137>
- [3] Chbihi A, Sauvage X, Blavette D (2012) Atomic scale investigation of Cr precipitation in copper. *Acta Mater* 60(11):4575–4585. <https://doi.org/10.1016/j.actamat.2012.01.038>
- [4] Goto M, Yamamoto T, Han SZ, Utsunomiya T, Kim S, Kitamura J, Ahn JH, Lim SH, Lee J (2021) Simultaneous increase in electrical conductivity and fatigue strength of Cu–Ni–Si alloy by utilizing discontinuous precipitates. *Mater Lett* 288:129353. <https://doi.org/10.1016/j.matlet.2021.129353>
- [5] Li GY, Li SY, Li L, Zhang DT, Wang JD, Tong YX (2021) A high strength and high electrical conductivity CuCrZr alloy prepared by aging and subsequent cryorolling. *Vacuum* 190:110315. <https://doi.org/10.1016/j.vacuum.2021.110315>
- [6] Li MM, Zinkle SJ (2012) Physical and mechanical properties of copper and copper alloys. Elsevier, Amsterdam
- [7] Wang X, Xiao Z, Qiu WT, Li Z, Liu F (2021) The evolution of microstructure and properties of a Cu–Ti–Cr–Mg–Si alloy with high strength during the multi-stage thermomechanical treatment. *Mater Sci Eng A* 803:140510. <https://doi.org/10.1016/j.msea.2020.140510>
- [8] Wei H, Chen YL, Zhao YN, Yu W, Su L, Tang D (2021) Correlation mechanism of grain orientation/microstructure and mechanical properties of Cu–Ni–Si–Co alloy. *Mater Sci Eng A* 814:141239. <https://doi.org/10.1016/j.msea.2021.141239>
- [9] Xie GL, Wang QS, Mi XJ, Xiong BQ, Peng LJ (2012) The precipitation behavior and strengthening of a Cu-2.0 wt% Be alloy. *Mater Sci Eng A* 558:326–330. <https://doi.org/10.1016/j.msea.2012.08.007>
- [10] Semboshi S, Ishikuro M, Sato S, Wagatsuma K, Takasugi T (2013) Extraction of precipitates from age-hardenable Cu–Ti alloys. *Mater Charact* 82:23–31. <https://doi.org/10.1016/j.materchar.2013.04.016>
- [11] Nagarjuna S, Balasubramanian K, Sarma DS (1995) Effects of cold work on precipitation hardening of Cu-4.5 mass% Ti alloy. *Mater Trans JIM* 36(8):1058–1066. <https://doi.org/10.2320/matertrans1989.36.1058>
- [12] Wendt H, Wagner R (1982) Mechanical properties of Cu–Fe alloys in the transition from solid solution to precipitation hardening. *Acta Metall* 30(8):1561–1570. [https://doi.org/10.1016/0001-6160\(82\)90176-6](https://doi.org/10.1016/0001-6160(82)90176-6)
- [13] Peng LJ, Xie HF, Huang GJ, Xu GL, Yin XQ, Feng X, Mi XJ, Yang Z (2017) The phase transformation and strengthening of a Cu-0.71 wt% Cr alloy. *J Alloys Compd* 708:1096–1102. <https://doi.org/10.1016/j.jallcom.2017.03.069>
- [14] Peng LJ, Xie HF, Huang GJ, Li YF, Yin XQ, Feng X, Mi XJ, Yang Z (2015) The phase transformation and its effects on properties of a Cu-0.12 wt% Zr alloy. *Mater Sci Eng A* 633:28–34. <https://doi.org/10.1016/j.msea.2015.02.077>
- [15] Jo HR, Kim JT, Hong SH, Kim YS, Park HJ, Park WJ, Park JM, Kim KB (2017) Effect of silicon on microstructure and mechanical properties of Cu–Fe alloys. *J Alloys Compd* 707:184–188. <https://doi.org/10.1016/j.jallcom.2016.12.352>
- [16] Lu DP, Wang J, Zeng WJ, Liu Y, Lu L, Sun BD (2006) Study on high-strength and high-conductivity Cu–Fe–P alloys.

- Mater Sci Eng A 421(1–2):254–259. <https://doi.org/10.1016/j.msea.2006.01.068>
- [17] Jeong YB, Jo HR, Kim JT, Hong SH, Kim KB (2019) A study on the micro-evolution of mechanical property and microstructures in (Cu-30Fe)-2X alloys with the addition of minor alloying elements. *J Alloys Compd* 786:341–345
- [18] Wu ZW, Chen Y, Meng L, Zhang Z (2021) Effect of Fe content on the microstructure and mechanical and electrical properties of Cu–Fe in situ composites. *J Mater Eng Perform* 30:5939–5946. <https://doi.org/10.1007/s11665-021-05579-6>
- [19] Spitzig WA, Chumbley LS, Verhoeven JD, Go YS, Downing HL (1992) Effect of temperature on the strength and conductivity of a deformation processed Cu-20% Fe composite. *J Mater Sci* 27(8):2005–2011. <https://doi.org/10.1007/BF01117911>
- [20] Dong QY, Wang MP, Shen LN, Jia YL, Li Z (2015) Diffraction analysis of α -Fe precipitates in a polycrystalline Cu–Fe alloy. *Mater Charact* 105:129–135. <https://doi.org/10.1016/j.matchar.2015.05.012>
- [21] Miura H, Tsukawaki H, Sakai T, Jonas JJ (2008) Effect of particle/matrix interfacial character on the high-temperature deformation and recrystallization behavior of Cu with dispersed Fe particles. *Acta Mater* 56(17):4944–4952. <https://doi.org/10.1016/j.actamat.2008.06.012>
- [22] Jeong YB, Jo HR, Park HJ, Kato H, Kim KB (2020) Mechanical properties and microstructural change in (Cu–Fe) immiscible metal matrix composite: effect of Mg on secondary phase separation. *J Mater Res Technol* 9(6):15989–15995. <https://doi.org/10.1016/j.jmrt.2020.11.049>
- [23] Shi GD, Chen XH, Jiang H, Wang ZD, Tang H, Fan YQ (2015) Strengthening mechanisms of Fe nanoparticles for single crystal Cu–Fe alloy. *Mater Sci Eng A* 636:43–47. <https://doi.org/10.1016/j.msea.2015.03.081>
- [24] Stepanov ND, Kuznetsov AV, Salishchev GA, Khlebova NE, Pantyrny VI (2013) Evolution of microstructure and mechanical properties in Cu–14% Fe alloy during severe cold rolling. *Mater Sci Eng A* 564:264–272. <https://doi.org/10.1016/j.msea.2012.11.121>
- [25] Verhoeven JD, Chueh SC, Gibson ED (1989) Strength and conductivity of in situ Cu–Fe alloys. *J Mater Sci* 24(5):1748–1752. <https://doi.org/10.1007/BF01105700>
- [26] Su JH, Liu P, Li HJ, Ren FZ, Dong QM (2007) Phase transformation in Cu–Cr–Zr–Mg alloy. *Mater Lett* 61(27):4963–4966. <https://doi.org/10.1016/j.matlet.2007.03.085>
- [27] Wang N, Li CR, Du ZM, Wang FM, Zhang WJ (2006) The thermodynamic re-assessment of the Cu–Zr system. *Calphad* 30(4):461–469. <https://doi.org/10.1016/j.calphad.2006.06.002>
- [28] Holzwarth U, Stamm H (2000) The precipitation behaviour of ITER-grade Cu–Cr–Zr alloy after simulating the thermal cycle of hot isostatic pressing. *J Nucl Mater* 279(1):31–45. [https://doi.org/10.1016/S0022-3115\(99\)00285-8](https://doi.org/10.1016/S0022-3115(99)00285-8)
- [29] Arias D, Abriata JP (1990) Cu–Zr (copper–zirconium). *J Phase Equilib* 11(5):452–459. <https://doi.org/10.1007/BF02898260>
- [30] Liu YL, Liu SH, Zhang C, Du Y, Wang J, Li YW (2017) Experimental investigation and thermodynamic description of the Cu–Zr system. *J Phase Equilib Diffus* 38(2):121–134. <https://doi.org/10.1007/s11669-017-0522-2>
- [31] Nakashima K, Miyamoto K, Kunimine T, Monzen R, Muramatsu N (2020) Precipitation behavior of Cu–Zr compounds in a Cu-0.13 wt% Zr alloy. *J Alloys Compd* 816:152650. <https://doi.org/10.1016/j.jallcom.2019.152650>
- [32] Dong QY, Shen LN, Cao F, Jia YL, Liao KJ, Wang MP (2015) Effect of thermomechanical processing on the microstructure and properties of a Cu–Fe–P alloy. *J Mater Eng Perform* 24(4):1531–1539. <https://doi.org/10.1007/s11665-014-1352-6>
- [33] Cao H, Min JY, Wu SD, Xian AP, Shang JK (2006) Pinning of grain boundaries by second phase particles in equal-channel angularly pressed Cu–Fe–P alloy. *Mater Sci Eng A* 431(1–2):86–91. <https://doi.org/10.1016/j.msea.2006.05.081>
- [34] Papaefthymiou S, Bouzouni M, Gavalas E (2018) Theoretical study of particle dissolution during homogenization in Cu–Fe–P alloy. *Metals* 8(6):455. <https://doi.org/10.3390/met8060455>
- [35] Yao Z, Ge J, Liu S (2006) Effect of doping with Zr on the properties of the deformation-processed Cu–Fe in-situ composites. *J Mater Sci* 41(12):3825–3829. <https://doi.org/10.1007/s10853-006-7941-5>
- [36] Zhuang XL, Lu S, Li LF, Feng Q (2020) Microstructures and properties of a novel γ' -strengthened multi-component CoNi-based wrought superalloy designed by CALPHAD method. *Mater Sci Eng A* 780:139219. <https://doi.org/10.1016/j.msea.2020.139219>
- [37] Zhu J, Titus MS, Pollock TM (2014) Experimental investigation and thermodynamic modeling of the co-rich region in the Co–Al–Ni–W quaternary system. *J Phase Equilib Diffus* 35(5):595–611. <https://doi.org/10.1007/s11669-014-0327-5>
- [38] Huang WL, Yu Y, Yang SY, Wang CP, Liu XJ, Kainuma R, Ishida K (2013) Experimental investigation of phase equilibria in the Cu–Fe–Zr ternary system. *J Phase Equilib Diffus* 34(6):438–446. <https://doi.org/10.1007/s11669-013-0257-7>
- [39] Wang YF, Gao HY, Han YF, Dai YB, Wang J, Sun BD (2017) First-principles study on the solubility of iron in dilute Cu–Fe–X alloys. *J Alloys Compd* 691:992–996. <https://doi.org/10.1016/j.jallcom.2016.08.247>

- [40] Yang HY, Bu YQ, Wu JM, Fang YT, Liu JB, Wang HT, Yang W (2021) CoTi precipitates: The key to high strength, high conductivity and good softening resistance in Cu-Co-Ti alloy. *Mater Charact* 176:111099. <https://doi.org/10.1016/j.matchar.2021.111099>
- [41] Yang HY, Bu YQ, Wu JM, Fang YT, Liu JB, Wang HT (2022) Nanocompound-induced anti-softening mechanisms: application to CuCr alloys. *Mater Sci Eng A*. <https://doi.org/10.1016/j.msea.2022.143038>
- [42] Dutkiewicz J (1977) Electron microscope study of the effect of deformation on precipitation and recrystallization in copper-titanium alloys. *Metall Trans A* 8(5):751–761. <https://doi.org/10.1007/BF02664785>
- [43] Zhang Y, Volinsky AA, Tran HT, Chai Z, Liu P, Tian BH, Liu Y (2016) Aging behavior and precipitates analysis of the Cu–Cr–Zr–Ce alloy. *Mater Sci Eng A* 650:248–253. <https://doi.org/10.1016/j.msea.2015.10.046>
- [44] Xiao XP, Huang J, Chen JS, Xu H, Li Z, Zhang JB (2018) Aging behavior and precipitation analysis of Cu–Ni–Co–Si alloy. *Crystals* 8(11):435. <https://doi.org/10.3390/cryst8110435>
- [45] Guy AG, Hren JJ (1974) *Elements of physical metallurgy*. Addison Wesley Publishing Company, Boston
- [46] Bass J (1972) Deviations from Matthiessen’s rule. *Adv Phys* 21(91):431–604. <https://doi.org/10.1080/00018737200101308>
- [47] Qian L, Zhou L, Pan ZY, Wang MP, Zhu X, Chang C (2010) Dynamics of phase transformation of Cu–Ni–Si alloy with super-high strength and high conductivity during aging. *Trans Nonferrous Met Soc China* 20(6):1006–1011. [https://doi.org/10.1016/S1003-6326\(09\)60249-1](https://doi.org/10.1016/S1003-6326(09)60249-1)
- [48] Gholami M, Altenberger I, Vesely J, Kuhn HA, Wollmann M, Janecek M, Wagner L (2016) Effects of severe plastic deformation on transformation kinetics of precipitates in CuNi3Si1Mg. *Mater Sci Eng A* 676:156–164. <https://doi.org/10.1016/j.msea.2016.08.099>
- [49] Le Bon A, Rofes-Vernis J, Rossard C (1975) Recrystallization and precipitation during hot working of a Nb-bearing HSLA steel. *Met Sci* 9(1):36–40. <https://doi.org/10.1179/030634575790444919>
- [50] Furuhashi T, Maki T (2001) Variant selection in heterogeneous nucleation on defects in diffusional phase transformation and precipitation. *Mater Sci Eng A* 312(1–2):145–154. [https://doi.org/10.1016/S0921-5093\(00\)01904-3](https://doi.org/10.1016/S0921-5093(00)01904-3)
- [51] Easterling KE, Miekko-Oja HM (1967) The martensitic transformation of iron precipitates in a copper matrix. *Acta Metall* 15(7):1133–1141. [https://doi.org/10.1016/0001-6160\(67\)90388-4](https://doi.org/10.1016/0001-6160(67)90388-4)
- [52] Fujii T, Kato M, Mori T (1991) Coarsening of incoherent α -Fe particles in a Cu–Fe alloy. *Mater Trans JIM* 32(3):229–236. <https://doi.org/10.2320/matertrans1989.32.229>
- [53] Newkirk JB (1957) Mechanism of precipitation in a Cu-2.5 pct Fe alloy. *JOM* 9(10):1214–1220. <https://doi.org/10.1007/BF03398294>
- [54] Rademacher T, Al-Kassab T, Kirchheim R (2009) The influence of elastic strain on the early stages of decomposition in Cu-1.7 at% Fe. *Ultramicroscopy* 109(5):524–529. <https://doi.org/10.1016/j.ultramic.2008.09.009>
- [55] Wang YF, Gao HY, Han YF, Dai YB, Wang J, Sun BD (2015) Role of the third element in accelerating Fe diffusivities in Cu from first principles. *J Alloys Compd* 639:642–647. <https://doi.org/10.1016/j.jallcom.2015.02.135>
- [56] Liu P, Kang BX, Cao XG, Huang JL, Yen B, Gu HC (1999) Aging precipitation and recrystallization of rapidly solidified Cu–Cr–Zr–Mg alloy. *Mater Sci Eng A* 265(1–2):262–267. [https://doi.org/10.1016/S0921-5093\(98\)01149-6](https://doi.org/10.1016/S0921-5093(98)01149-6)
- [57] Ban YJ, Geng YF, Hou JR, Zhang Y, Zhou M, Jia YL, Tian BH, Liu Y, Li X, Volinsky AA (2021) Properties and precipitates of the high strength and electrical conductivity Cu–Ni–Co–Si–Cr alloy. *J Mater Sci Technol* 93:1–6. <https://doi.org/10.1016/j.jmst.2021.03.049>
- [58] Wang CY, Cepeda-Jimenez CM, Pérez-Prado MT (2020) Dislocation-particle interactions in magnesium alloys. *Acta Mater* 194:190–206. <https://doi.org/10.1016/j.actamat.2020.04.055>
- [59] Song M (2007) Modeling the hardness and yield strength evolutions of aluminum alloy with rod/needle-shaped precipitates. *Mater Sci Eng A* 443(1–2):172–177. <https://doi.org/10.1016/j.msea.2006.08.025>
- [60] Chu QL, Zhang M, Li JH, Yan FX, Yan C (2018) Investigation of microstructure and fracture toughness of Fe–Zr welded joints. *Mater Lett* 231:134–136. <https://doi.org/10.1016/j.matlet.2018.08.038>
- [61] Li J, Huang GJ, Mi XJ, Peng LJ, Xie HF, Kang YL (2019) Microstructure evolution and properties of a quaternary Cu–Ni–Co–Si alloy with high strength and conductivity. *Mater Sci Eng A* 766:138390. <https://doi.org/10.1016/j.msea.2019.138390>
- [62] Edwards DJ, Singh BN, Tähtinen S (2007) Effect of heat treatments on precipitate microstructure and mechanical properties of a CuCrZr alloy. *J Nucl Mater* 367:904–909. <https://doi.org/10.1016/j.jnucmat.2007.03.064>
- [63] Sim GM, Ahn JC, Hong SC, Lee KJ, Lee KS (2005) Effect of Nb precipitate coarsening on the high temperature strength in Nb containing ferritic stainless steels. *Mater Sci Eng A* 396(1–2):159–165. <https://doi.org/10.1016/j.msea.2005.01.030>

- [64] Lengeler B, Schilling W, Wenzl H (1970) Deviations from Matthiessen's rule and longitudinal magnetoresistance in cold-worked and neutron-irradiated copper. *J Low Temp Phys* 2(2):237–254. <https://doi.org/10.1007/BF00628179>
- [65] Andrews PV, West M, Robeson CR (1969) The effect of grain boundaries on the electrical resistivity of polycrystalline copper and aluminium. *Philos Mag* 19(161):887–898. <https://doi.org/10.1080/14786436908225855>
- [66] Liu X (1982) Mechanical and physical properties of cast alloys. Mechanical Industry Press, Beijing (**in Chinese**)

Publisher's Note Springer Nature remains neutral with regard to jurisdictional claims in published maps and institutional affiliations.

Springer Nature or its licensor (e.g. a society or other partner) holds exclusive rights to this article under a publishing agreement with the author(s) or other rightsholder(s); author self-archiving of the accepted manuscript version of this article is solely governed by the terms of such publishing agreement and applicable law.